ROYAL SOCIETY
OF CHEMISTRY

PAPER

Check for updates

Enantiorecognition in a multi-component environment†

Joanna Mazurkiewicz, [ID] [ab] Ewa Stanek, [ID] [bc] Pedro Maximiano, [ID] [d]
Tiago H. Ferreira, [ID] [d] Marta Karpiel, [ID] [ab] Szymon Buda, [ID] [a]
Justyna Kalinowska-Tłuścik, [ID] [a] Pedro N. Simões, [ID] [d] Igor Reva [ID] [d] and
Agnieszka Kaczor [ID] *[a]

We demonstrate that enantiopreference in the binding of *S,S* over *R,R* astaxanthin (AXT) to albumin manifests itself only for racemic (but not enantiopure) carotenoids. The observed enantioselectivity is rationalized using chiroptical spectroscopies supported by molecular docking, molecular dynamics and quantum-chemical calculations. These methods offer a plausible explanation for the observed enantiopreference, as they reveal a unique binding mode of the (3*S*,3′*S*)-AXT form with the protein in contrast to multiple (random) possibilities for albumin binding with the (3*R*,3′*R*)-AXT, and also a higher interaction energy of the latter enantiomer with the protein.

1. Introduction

Enantiorecognition is important in chiral separation,[1,2] drug binding,[1] and enzymatic catalysis.[3] Usually, chiral recognition is analysed in model systems where the interaction of a single enantiomer with another chiral entity is considered. In such simple supramolecular systems (two chiral entities and a solvent), the preference in the interaction of one enantiomer with another chiral unit is recurring and often evident. The real biological systems are, however, multicomponent and dynamic assemblies, shaped usually by multiple additive non-covalent interactions,[4] where two interacting chiral entities are surrounded by multiple other molecules in their environment. The advantage of such loose aggregates is their flexibility, in turn generating structures governed by kinetic, rather than thermodynamic factors,[5,6] and occasionally expressing indeterministic behaviour.[7–9]

Carotenoids are the second most abundant group of pigments in nature. Many carotenoids are chiral, but the relationship between their handedness and bioavailability or bioactivity is poorly understood. As carotenoids are lipid-soluble tetraterpenoids, they are preferably stored in adipocytes (fat cells).[10] It has

been established that the uptake of carotenoids to adipocytes requires transporters.[11] Albumins are efficient nanocarriers of carotenoids due to the intermediate binding constants of carotenoids and albumins.[12] Recently, we have demonstrated that the efficient delivery of carotenoids to adipocytes originates in a hydrophobic periphery area in domain IIIB of albumin that loosely binds pigment molecules in aqueous media and enables their easy detachment in hydrophobic environments.[13]

In this study, aiming to understand the impact of chirality on the carotenoid–albumin binding and delivery to adipocytes, we have considered the enantiorecognition of a model chiral carotenoid astaxanthin (3,3′-dihydroxy-β,β-carotene-4,4′-dione, AXT) binding to bovine serum albumin (BSA). We have made a puzzling observation that the enantiomeric preference in pigment–protein binding considerably depends on the level of complexity of the system. Although no evident enantioselectivity has been observed for complexes of albumin with enantiopure AXT, the components of multielement racemic AXT interact with the protein differently, resulting in enantiopreference confirmed *via* the preferential uptake of protein-bound (3*R*,3′*R*)-AXT by primary murine adipocytes. We demonstrate that the observed differences can be explained based on binding modes and energies of interactions of AXT enantiomers with the protein.

2. Experimental

2.1. Separation of enantiopure (3*S*,3′*S*)-AXT and (3*R*,3′*R*)-AXT from racemic mixtures

(3*S*,3′*S*)-AXT and (3*R*,3′*R*)-AXT were obtained from the separation of the racemic mixture of AXT [(*rac*)-AXT, Sigma Aldrich]

[a] *Faculty of Chemistry, Jagiellonian University, 2 Gronostajowa Str., Krakow 30-387, Poland. E-mail: agnieszka.kaczor@uj.edu.pl*

[b] *Doctoral School of Exact and Natural Sciences, Jagiellonian University, 11 Lojasiewicza Str., Krakow 30-348, Poland*

[c] *Jagiellonian Centre for Experimental Therapeutics (JCET), Jagiellonian University, 14 Bobrzynskiego Str., Krakow 30-348, Poland*

[d] *CERES, Department of Chemical Engineering, University of Coimbra, R. Sílvio Lima, Coimbra 3030-790, Portugal*

using the process of converting (*rac*)-AXT into dicamphanate, and then separation of diastereoisomers on preparative thin layer chromatography (PTLC). A solution of 600 mg (1 mmol) of (*rac*)-AXT in 8 mL of pyridine was cooled to 0 °C under argon and mixed with 550 mg (2.5 mmol) of (−)-camphanoyl chloride. Then the ice bath was removed, and the mixture was stirred for about 10 minutes. The reaction progress was monitored by TLC (dichloromethane (DCM)/diethyl ether (Et_2O) 9 : 1). Then, 25 mL of water was added dropwise, causing the mixture to crystallize out. After filtration, the dark solid was washed several times with water and then with hexane. After drying at room temperature, 907 mg (95%) of a loose, reddish-brown powder was obtained. A mixture of 30 mg of (*rac*)-AXT di-(−)-camphanate in 1 mL of DCM was added onto a PTLC plate. A mixture of toluene/acetone 9 : 1 (v/v) was used for elution. Two single isomers were separated, (3*R*,3′*R*)-AXT di-(−)-camphanate 5.6 mg, and (3*S*,3′*S*)-AXT di-(−)-camphanate 4.2 mg. Chromatographic separation was repeated several times. To a solution of 46 mg (48 μmol) of (3*R*,3′*R*)-AXT di-(−)-camphanate in 3 mL of methylene chloride at room temperature, 3 mL of methanol were added under argon. While stirring, 120 μL of 1N aqueous NaOH was added. The reaction progress was monitored by TLC (DCM/Et_2O 9 : 1). After about 16 hours, the mixture was reduced to half the volume without heating, causing the product to crystallize. The filtered material was thoroughly washed several times with methanol (4 × 2 mL) and finally washed once with hexane (2 mL) to give 6.8 mg (11.4 μmol, 24%) of pure (3*R*,3′*R*)-AXT. Hydrolysis of pure (3*S*,3′*S*)-astaxanthin di-(−)-camphanate (39 mg, 40,7 μmol) gave 5.9 mg (9.9 μmol, 24%).

2.2. AXT–BSA complex preparation

(3*S*,3′*S*)-AXT : BSA, (3*R*,3′*R*)-AXT : BSA and (*rac*)-AXT : BSA [(*rac*)-AXT, obtained from Sigma Aldrich or Carbosynth] complexes were prepared in a similar way to our previous work,[13] based on an appropriately modified protocol described earlier.[14] The appropriate forms of AXT dissolved in tetrahydrofuran (THF, Thermo Fisher Scientific) with 10 μM solution of BSA (fatty acid-free, Sigma-Aldrich) in phosphate buffered saline (PBS, Thermo Fisher Scientific) were mixed to obtain systems with molar ratios of AXT to BSA equal to 1 : 1 and 3 : 1. The final concentration of THF in the water phase was 2% (by volume). The prepared samples were incubated for 1 h at 37 °C with continuous stirring and then stored for 12 h in a refrigerator (at 4 °C). To remove (a minor amount) possible AXT aggregates that were not attached to the protein, the samples were centrifuged at 20 °C at 15 000 rpm for 20 minutes before the measurements, as previously reported in ref. 14. For comparative purposes, 10 and 30 μM solutions of (3*S*,3′*S*)-AXT, (3*R*,3′*R*)-AXT and (*rac*)-AXT in THF were also prepared and characterized, as well as 10 μM BSA solution in PBS.

2.3. ECD measurements

Electronic absorption and electronic circular dichroism (ECD) spectra were registered in two ranges: 200–300 nm (far UV) and 300–700 nm (UV-vis), using a Jasco J-1500 spectrometer (with JASCO 1.52.00 software). For the 200–300 nm range, all samples

were diluted 20-fold before the measurements, whereas for the 300–700 nm range, the samples of AXT : BSA complexes were measured undiluted, and the samples of AXT dissolved in THF were measured after 2-fold [(*rac*)-AXT] or 3-fold [(3*S*,3′*S*)-AXT, (3*R*,3′*R*)-AXT] dilution to keep the absorbance peak below 1.5 and avoid saturation. For the 200–300 nm range, the optical path length of 1 mm and the scan speed of 50 nm min⁻¹ with 0.2 nm data pitch were used. For the 300–700 nm range, these parameters were 10 mm, 50 nm min⁻¹, and 0.5 nm, respectively. The obtained spectra are the result of the accumulation of 8 individual scans for the far UV range and 5 individual scans for the UV-vis region. After subtracting the spectra of the appropriate solvents from the spectra of the samples, the spectra were additionally smoothed in Origin Pro® 2021b.

2.4. ROA measurements

Resonance Raman optical activity (RROA) and resonance Raman (RR) measurements were performed using the BioTools Inc. ChiralRAMAN-2x spectrometer equipped with a CCD camera and 532 nm excitation wavelength (with ROA Display and Control 4.2.0.0 software). The Raman and RROA spectra of AXT : BSA complexes and all tested forms of AXT dissolved in THF were registered in the 500–2500 cm⁻¹ range, with 1 h acquisition time, 30 mW or 16 mW laser power, and an illumination period of 3.087 or 0.5145 s, respectively. Averaging of the obtained RROA and RR spectra and baseline correction were performed using the OPUS 7.2 program.

2.5. Cell preparation

Epididymal white adipose tissue (eWAT) was isolated from 24 week-old male C57Bl/6J mice (n = 3 per each experiment) (Medical University of Warsaw, Warsaw, Poland), minced and kept for 1 h in the enzymatic solution (3.5 mg mL⁻¹ collagenase D (Roche Holding AG, Basel, Switzerland), 2% BSA (Sigma-Aldrich), and 150 μM $CaCl_2$ dissolved in PBS) at a temperature of 37 °C with mild shaking (every 10 minutes). Then, digestion tissue remnants were filtrated through a 100 μm nylon cell strainer. Subsequently, the separated primary adipocytes were resuspended in cell culture medium (DMEM:F12, 8 μg mL⁻¹ biotin, and 50 μg mL⁻¹ gentamycin) that contained additionally one of the following additives: (3*S*,3′*S*)-AXT : BSA complex (with molar ratio of AXT to BSA equal to 3 : 1), (3*R*,3′*R*)-AXT : BSA complex (molar ratio 3 : 1), and (3*S*,3′*S*)-AXT dissolved in THF or (3*R*,3′*R*)-AXT dissolved in THF. The final AXT concentration given to the adipocytes was 10 μM for all four prepared groups. Stimulation of the primary adipocytes with the carotenoid was carried out at 37 °C, 5% CO_2 in a cell culture incubator under light-protected conditions and kept in the dark. After stimulation, to perform Raman imaging, cells were placed between the CaF_2 microscope slide and the coverslip and measured at selected time points. The experiments were repeated 2 times. The studies were performed on isolated cells from mice sacrificed under anaesthesia. Mice were not subjected to any vital procedures; therefore, ethical approval was not required. All experimental procedures involving animals were conducted according to the Guidelines for Animal Care and Treatment

4906 | *Phys. Chem. Chem. Phys.*, 2025, **27**, 4905–4914

This journal is © the Owner Societies 2025

of the European Communities and the Guide for the Care and Use of Laboratory Animals published by the US National Institute of Health (NIH publication no. 85–23, revised 1996).

2.6. Raman microscopy

A confocal Raman microscope (WITec alpha300, Ulm, Germany) equipped with a 532 nm laser, a UHTS 300 spectrograph (600 grooves mm^{-1} grating), and a CCD detector (DU401A-BV-352, Andor, UK) was used for cell measurements. Raman spectra were collected using low laser power to avoid reducing the AXT signal, and with 1 μm sampling density in x/y directions and a 0.2 s exposure time per spectrum. Cells were measured using a 20× air objective (NA = 0.45, Nikon CFI S Plan Fluor ELWD, Japan) after placing under the coverslip on CaF$_2$ glass slides. WITec Project Plus 5.1 software was used for baseline correction (using automatic polynomial regression of degree 3) and cluster analysis (KMCA, *i.e.*, the *k*-means method using the Manhattan distance, WITec Project Plus). Cluster analysis was performed to extract the average Raman spectra of whole adipocytes (class rich in lipids) from the whole image. All spectra were normalized using vector normalization in the 1800–600 cm^{-1} range with the OPUS 7.2 program.

3. Calculations

3.1. Molecular dynamics (MD) simulations

All-atom MD simulations were performed to investigate the behaviour of (3S,3′S)-AXT : BSA, (3R,3′R)-AXT : BSA, (3R,3′S)-AXT : BSA and (3S,3′R)-AXT : BSA systems for the 3 : 1 molar ratio, using the GROMACS 2021.5 software.[15] The coordinates of the AXT : BSA complexes resulting from the docking calculations were used as a starting point for building the simulation box, by adding neutralizing Na$^+$ counterions and the remaining two AXT molecules at random positions. The box was solvated with a mixture of water and THF molecules, at the experimental composition of 2.0% v/v THF. Following an initial energy minimization, the system was equilibrated in the NPT ensemble at 37 °C and 1.0 bar leading to an average side length of the cubic simulation box of *ca.* 13.4 nm. Finally, data were gathered from production runs for a total of 2.0 μs physical time to ensure appropriate sampling of relevant phase space configurations. The production runs were performed in the NPT ensemble under the same conditions as equilibration by using the V-rescale thermostat[16] and the Parrinello–Rahman barostat.[17,18] All interactions involving BSA, AXT were modelled by the CHARMM36m[19] force field (FF) and those for THF by CGenFF[20] whose parameters were obtained automatically *via* the CHARMM–GUI interface.[21] Internal rotations around selected single bonds (C8–C9, C10–C11, C12–C13, and C14–C15) were restrained to maintain a fully elongated, transoid conformation of the AXT molecules.[13,22] The restraints were such that the rotational energy barrier would match that calculated for the AXT molecule in vacuum at the B3LYP/6-31G(d) level of theory (21.6 kJ mol^{-1}). The TIP3P model[23] was used to describe interactions involving water molecules.

The leapfrog algorithm was used to integrate the equations of motion, with a time step of 2.0 fs (achieved by restraining bonds involving H-atoms *via* the LINCS algorithm[24]) and under full periodic boundary conditions. All nonbonded interactions were truncated at a cutoff radius of 1.2 nm, while force switching and particle mesh Ewald (PME)[25] algorithms were used to apply long-range corrections. The analysis of the trajectories was performed with GROMACS native tools, whereas the program VMD 1.9.4a55[26] was used for visualizing the trajectories.

3.2. Quantum-chemical calculations (modelling of ECD spectra)

Properties of the low-energy electronic excited states were computed using the time-dependent (TD) density functional theory (DFT) method,[27,28] with the Becke's three-parameter exchange functional,[29] the non-local correlation functional of Lee, Yang, Parr (LYP),[30] and the Vosko, Wilk, Nusair (VWN) functional III for local correlation.[31] This three-parameter density functional, known as B3LYP, combined with the standard 6-31G(d,p) basis set,[32–34] was applied in these calculations. The ECD analysis was also performed during the TD-DFT calculations. The ECD theoretical computations reported here were carried out with the Gaussian 16 set of programs.[35] The systems intended for the ECD analysis consisted of dimers, composed of two monomeric AXT units having the chosen chiralities. The structures of dimers were extracted from the MD trajectories, based either on time (along the MD trajectory) or on the proximity criteria (the distance between centres of mass and the angle between the vectors formed by C7 and C7′ pairs of atoms in each of two AXT molecules). The geometries of AXT dimers extracted from the MD runs were not optimized, and the ECD calculations were carried out on these frozen geometries. For the graphical representation of ECD spectra, each computed electronic transition was convoluted with a Lorentzian function having a half width at half-maximum (hwhm) equal to 1000 cm^{-1} (0.124 eV), using the GaussView software.[36]

3.3. Molecular docking procedures

For the docking study, the apo-BSA crystal structure was selected based on the best resolution criterion and downloaded from the Protein Data Bank (https://www.rcsb.org/).[37] The available highest resolution X-ray diffraction data for BSA crystals were collected at 2.47 Å for PDB ID 4F5S.[38] The protein and ligands' structures were pre-processed using the Maestro 13.4 integrated software[39] by adding hydrogen atoms, fixing side chains, and minimizing the energy of ligand structure using the OPLS4 Force Field.[40] Molecular docking was performed in GOLD 2021.3.0 (genetic optimization for ligand docking) software[41] using a semi-flexible docking module and Chemscore scoring function. However, due to the strong resonance effect in the carbon chain, which is acclaimed for this class of compounds, rotation around selected single bonds (C8–C9, C10–C11, C12–C13, C14–C15 and their corresponding symmetry-equivalent mirror bonds, shown in Scheme 1) was prohibited to maintain the fully elongated, transoid conformation of the molecule. According to our previous docking studies,[13] the centre of the docking sphere was set at Leu346 with a radius of 15 Å and included residues of the binding site

This journal is © the Owner Societies 2025

Phys. Chem. Chem. Phys., 2025, **27**, 4905–4914 | **4907**
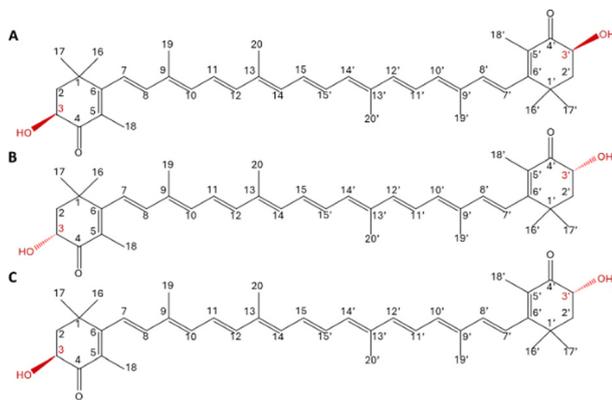
Scheme 1 Molecular structures of AXT stereoisomers. (3S,3′S)-AXT (**A**), (3R,3′R)-AXT (**B**), and *meso* = (3S,3′R)-AXT = (3R,3′S)-AXT (**C**). Note solid-wedge and dash-wedge bonds at positions 3 and 3′.

corresponding to human serum albumin with an affinity towards ibuprofen.[42] Molecular docking experiment with the *meso* AXT monomer was conducted and the best-scored 200 poses were recorded to obtain the statistically significant observation for the preference in binding of the S or R-end to the deep region of the binding site. For simulations with the (3R,3′R)-AXT and (3S,3′S)-AXT molecules, 20 of the best-scored poses were recorded. The applied docking protocols were tested using ibuprofen as a reference ligand. Analysis and visualization of the docking results were conducted using PyMOL Molecular Graphics System 2.4.1[43] and protein–ligand interaction profiler (PLIP) server.[44]

4. Results and discussion

4.1. Complexes of albumin with enantiopure astaxanthin

Scheme 1 shows the molecular structures of AXT stereoisomers. The electronic absorption and the ECD spectra of the complexes of BSA with AXT enantiomers (3S,3′S)-AXT and (3R,3′R)-AXT are presented in Fig. 1.

The hypsochromic shift of the $\pi \to \pi^*$ electronic absorption band (Fig. 1A) compared to that of the AXT monomer (Fig. S1, ESI†) and the characteristic intense exciton couplet in the ECD[45–49] (Fig. 1B) demonstrate that hydrogen-bonded (H-bonded) *H2*-aggregates of AXT are formed due to the interaction of the enantiopure AXT with the protein. Independent of the carotenoid concentration (1:1 or 3:1 AXT:BSA), the ECD spectra are almost mirror images for both forms, showing that there is no significant preference in binding of AXT enantiomers to albumin in the studied systems. In agreement with ECD, resonance Raman optical activity (RROA) spectra also show the mirror image relationship for both enantiomers for both AXT:BSA systems (Fig. 1D).

About a 1:3 signal intensity ratio is maintained in the Raman spectra (Fig. 1C) of 1:1 to 3:1 complexes, but a 1:9 signal intensity is observed in RROA (Fig. 1D and Table S1, ESI†). We have demonstrated previously that RROA detects aggregates selectively in the presence of monomers.[22,47]
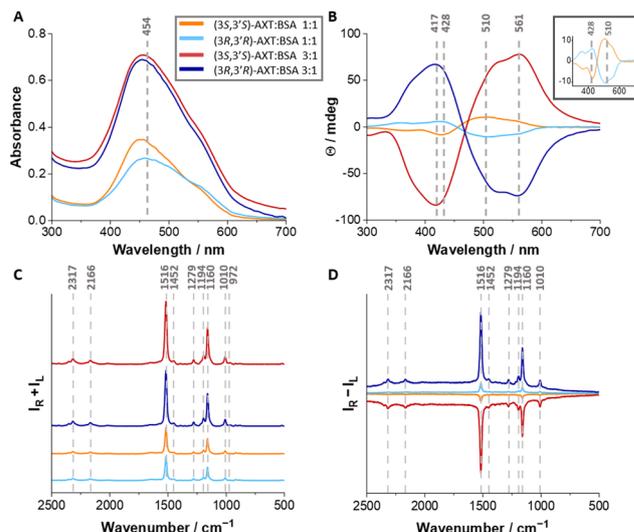

Fig. 1 Complexes of albumin with enantiopure astaxanthin show no preference in binding of (3S,3′S) or (3R,3′R) stereoisomers with BSA. Electronic absorption (**A**), ECD (**B**), Raman (**C**), and RROA (**D**) spectra of AXT:BSA complexes. The spectra were measured for two molar ratios of AXT to BSA equal to 1:1 and 3:1 (C_{AXT} = 10 and 30 μM; C_{BSA} = 10 μM). The inset in part **A** shows colour codes for different molar ratios and chiralities. The inset in part **B** shows a close-up of the ECD spectra for the AXT:BSA 1:1 system.

Therefore, the overly increased RROA intensity of the 3:1 complex compared to the resonance Raman intensity is likely a result of the increased size of aggregates in the 3:1 AXT:BSA system compared to the 1:1 ones. Other observations confirm a lack of differences in enantiomer behaviour in the enantiopure AXT:BSA systems. The complex is very stable in time and its stability does not differ for enantiomers (Fig. S2 and S3, ESI†). Moreover, the albumin structure is equally unaffected due to the carotenoid binding (Fig. S4, ESI†). Overall, no enantioselectivity in binding of AXT enantiomers to albumin is detected for enantiopure AXT-albumin systems. Quite a different picture is obtained for racemic AXT-albumin assemblies.

4.2. Enantiorecognition in albumin–(racemic AXT) complexes

The AXT racemate ((*rac*)-AXT) is composed of the (3S,3′S), *meso*, and (3R,3′R) forms in the 1:2:1 proportion, respectively. The maximum of the electronic absorption band in (*rac*)-AXT in THF in the monomeric form is observed at 478 nm (Fig. S5, ESI†). The 1:1 and 3:1 AXT:BSA complexes were prepared in several independent experiments. The signal obtained in any of the single experiments is highly repeatable (Fig. 2).

The results obtained for nine repetitions of the experiment, for both 1:1 and 3:1 AXT:BSA ratios, are shown in Fig. 3. The maximum of the $\pi \to \pi^*$ band in (*rac*)-AXT:BSA complexes (Fig. 3A and B) is observed at different wavelengths, but in all cases the band is broadened and is either hypso- or/and batochromically shifted relative to the band of the monomer (Fig. S5, ESI†), implying that aggregates are formed.[45–49] For both 1:1 and 3:1 AXT:BSA systems, ECD spectra (Fig. 3C and D) show approximately one of the following shapes: close to zero-
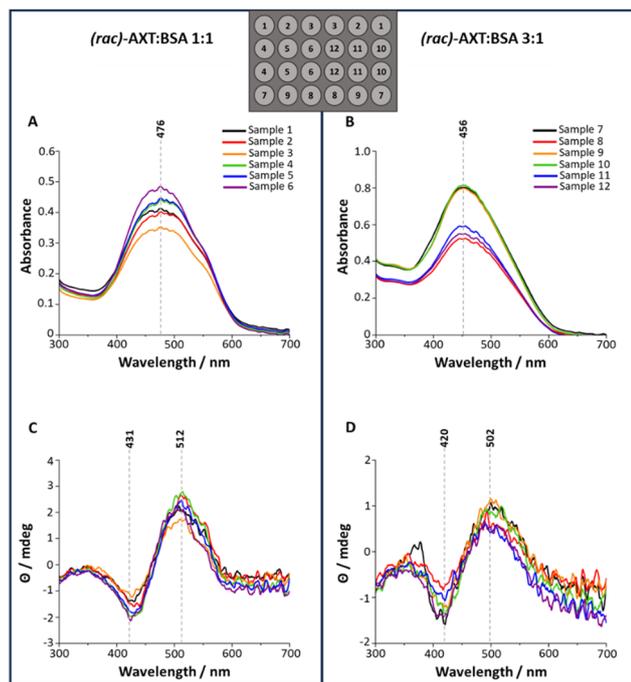
4908 | *Phys. Chem. Chem. Phys.*, 2025, **27**, 4905–4914

This journal is © the Owner Societies 2025

Fig. 2 Electronic absorption and ECD spectra of (*rac*)-AXT : BSA complexes for a single sample (experiment) after incubating in different positions in the thermoshaker (intra-experiment variability). The electronic absorption spectra (**A**) and (**B**), and ECD spectra (**C**) and (**D**) of the AXT : BSA complexes measured for two molar ratios of AXT to BSA equal to 1 : 1 and 3 : 1, respectively (C_{AXT} = 10 and 30 μM; C_{BSA} = 10 μM).
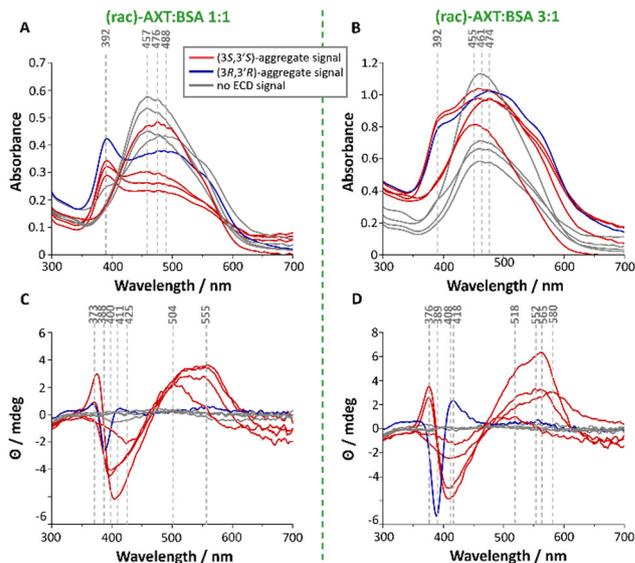

Fig. 3 Enantiorecognition in complexes of albumin with racemic astaxanthin in nine independent experiments (inter-experiment variability). Electronic absorption (**A**) and (**B**) and ECD (**C**) and (**D**) spectra of AXT : BSA complexes prepared from (*rac*)-AXT. The complexes were measured for two molar ratios of AXT to BSA equal to 1 : 1 and 3 : 1 (C_{AXT} = 10 and 30 μM; C_{BSA} = 10 μM). Different types of observed spectra denoted in different colours.

intensity ECD (denoted in grey) or a complicated exciton signal (denoted in red or blue). This means that for both AXT : BSA ratios in over half of the experiments the (*rac*)-AXT : BSA systems generate the exciton ECD signal derived from the racemic carotenoid. The intensity of the signal and its shape differ, yet it shows certain regularities. The signal is considerably less intense than the signal of the enantiopure AXT : BSA (Fig. 1B).

For the systems that show non-zero ECD, the signal consists of couplets characteristic either of typical *H*-aggregates (the low-wavenumber couplet, intersection point at *ca.* 380 nm), or—more often—the mixture of *H* and *H2*/*J*-assemblies (the high-wavenumber broad couplet, intersection point at *ca.* 470 nm).[46] *H2* and *J*-aggregates are both related with a very broad excitonic couplet and are difficult to clearly discriminate between,[46] hence we use the *H2*/*J* notation. The disorder of the system is underlined by the different ratio of *H* and *H2*/*J*-aggregates in systems showing induced ECD.

To rationalize this paradoxical result, we used molecular docking, molecular dynamics, and quantum-chemical calculations.

4.3. Different scenarios of binding to proteins for different AXT stereoisomers

For molecular dynamics simulations, all initial supermolecular systems were built from three AXT molecules and BSA in such a way that one AXT was placed in the binding pocket of BSA—in the Leu346 region—and two other AXT molecules were introduced randomly in the simulation box. Importantly, for the

meso structure, we considered both the *S*-end (($3R,3'S$)-AXT : BSA) and the *R*-end (($3S,3'R$)-AXT : BSA) of AXT interacting with the deep regions of the binding pocket. Overall, two different scenarios are possible (Fig. 4).

In Scenario 1 (Fig. 4B, left), one AXT molecule stays in the binding pocket and two other AXT molecules form an *H*-type dimer in the IIIB domain. This scenario is consistently predicted by MD simulations for binding of ($3S,3'S$)-AXT and ($3R,3'S$)-AXT forms (with the *S*-end of AXT in the deep region of the BSA's binding pocket), and only one (of the three independent MD runs) for the ($3R,3'R$)-AXT complex with BSA. This is proven by the computed distances between the centres of mass (COM) of each AXT molecule and the binding pocket, and by the distances between the COMs of each AXT molecule, shown in Fig. 5. A proximity of less than 1 nm between the COMs of the AXT1 molecule and the BSA binding pocket means that it stays in the latter (see red traces in Fig. 5A). The longer distances (*ca.* 6 nm) for the other two AXT molecules mean that they remain on the periphery of BSA (see the green and blue traces in Fig. 5A).

This condition is always fulfilled when the *S*-end of AXT is in the binding pocket (Fig. 5A, first column). It is confirmed by the pairwise distances between COMs of AXT molecules. Fig. 5B (third column, *S*-end in the binding pocket) shows a steady distance of *ca.* 1 nm between COMs of AXT2 and AXT3 after 1 μs, meaning that they form a dimer (see the blue traces in Fig. 5B) and both are far away from AXT1 (red and black traces in Fig. 5B). The ($3R,3'R$)-AXT : BSA system behaves differently compared with the ($3S,3'S$)-AXT : BSA one, showing stochasticity. This is evidenced by the very disparate pattern of the distance plots across the different systems where the *R*-end is
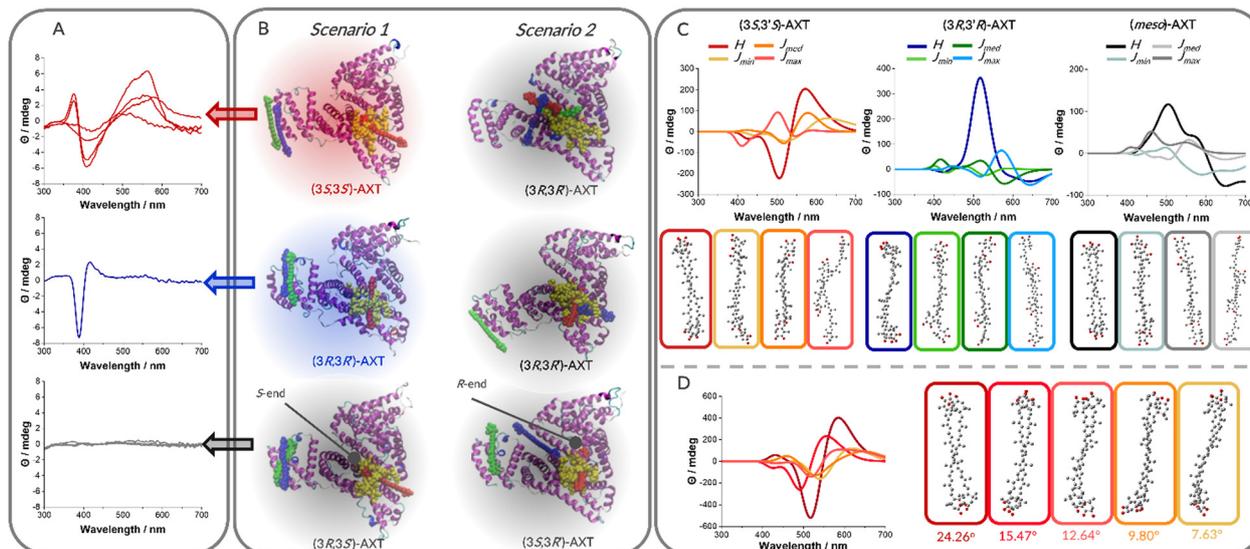
This journal is © the Owner Societies 2025

Phys. Chem. Chem. Phys., 2025, **27**, 4905–4914 | **4909**

Fig. 4 Stereoselectivity in AXT binding to albumin. Different binding modes of AXT to BSA predicted by MD simulations (**B**) explain the observed experimental spectra (**A**). (**B**) In Scenario 1, one AXT lodges in the binding pocket and two other AXT molecules form an *H*-type dimer. In Scenario 2, AXT molecules aggregate into loosely bound *J*-type dimers or a trimer. The calculated ECD spectra (unscaled, B3LYP/6-31G(d,p)) show that only *H*-dimers of either (3*S*,3'*S*)-AXT or (3*R*,3'*R*)-AXT type provide an intense signal (**C**) and the signal generated by the *H*-dimers depends on the dimers' helicity expressed as the angle between the vectors formed by C7 and C7' pairs of atoms in each of two AXT molecules making a dimer (**D**, representative structures). All analysed structures are shown in Fig. S7 (ESI†).

inside the binding pocket, as shown in Fig. 5, second and fourth columns. It must be noted that, in one of the independent runs of the (3*R*,3'*R*)-AXT : BSA system the binding pocket had opened, after which the bound AXT1 molecule migrated outside of it, as can be seen by the increase in its distance from the biding pocket (Fig. 5, second column, first row).
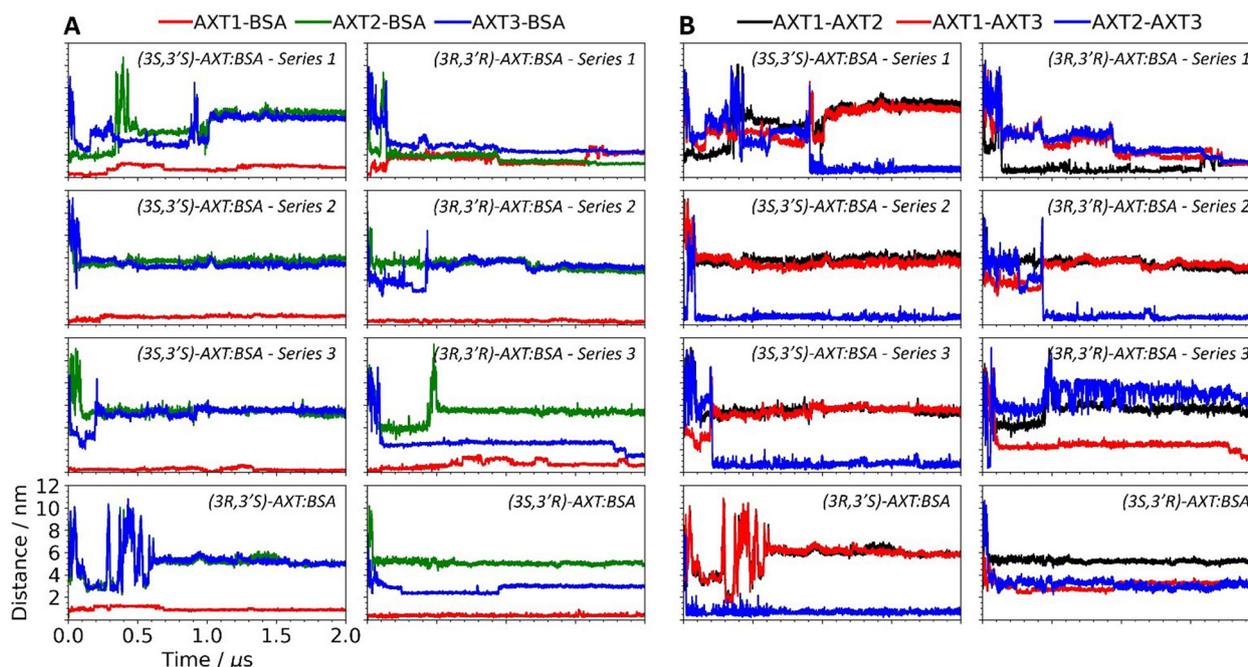

Fig. 5 (**A**) (First and second columns): distances between the centres of mass (COM) of the individual AXT molecules and COM of the BSA binding pocket residues. (**B**) (Third and fourth columns): pairwise distance between COMs of the AXT molecules. For (3*S*,3'*S*)-AXT : BSA and (3*R*,3'*R*)-AXT : BSA, the results of three independent series are shown (both in (**A**) and (**B**)). AXT1 is the AXT molecule initially placed inside the binding pocket (AXT coloured red in Fig. 4B), while AXT2 and AXT3 are the molecules initially placed outside (AXT coloured green and blue, respectively, in Fig. 4B). See the legend at the top for the colour codes.

Concomitantly, a trimer was loosely formed by the AXT molecules outside of the binding pocket. The opening of the binding pocket was naturally accompanied by large fluctuations in its residues, as clearly demonstrated in Fig. S6 (ESI†), which shows the large root mean square deviation (RMSD) values exhibited in series 1 of $(3R,3'R)$-AXT : BSA (yellow colour). Fig. S6 (ESI†) also highlights the stochastic nature of the $(3R,3'R)$-AXT : BSA system, as all three independent runs resulted in very different fluctuation patterns for the binding pocket (and, therefore, different stabilities), featuring overall RMSD values ranging from very low (0.2–0.4 nm, series 3, Fig. S6E, ESI†) up to very high (up to 0.8 nm, series 1, Fig. S6G, ESI†). For all other enantiomers, the binding pocket remains relatively stable, generally featuring small RMSD values.

Scenario 2 consists in the formation of very loosely interacting J-type assemblies. They can be trimers (top-right $(3R,3'R)$-AXT : BSA in Fig. 4B) or dimers (middle-right $(3R,3'R)$-AXT : BSA and bottom-right $(3S,3'R)$-AXT : BSA in Fig. 4B). This behaviour is predicted by MD simulations for complexation of $(3R,3'R)$-AXT (two out of three cases) and of $(3S,3'R)$-AXT stereoisomers with albumin. The existence of different binding scenarios raises the question of how they are related to the ECD signal. To address this question, we considered the general ECD shape and intensity of J-like and H-like AXT aggregates (Fig. 4C) predicted by MD (Fig. 5). H and J-aggregates were selected based on the distances between COM along with the degree of parallel alignment of the molecules that form the dimer, assuming the increase in the "J-character" with the increase of the distance between COM and parallel alignment. The analysis of selected structures demonstrates that only $(3S,3'S)$-AXT or $(3R,3'R)$-AXT H-type dimers provide an intense ECD signal. Furthermore, for different H-dimers (Fig. 4D and Fig. S7, ESI†) the key parameter dictating the intensity is the helicity of the structure (expressed as the angle between the vectors formed by C7 and C7′ pairs of atoms in each of two AXT molecules building a dimer) with the positive couplet generated for left-handed dimers and *vice versa*.

So, the signal observed experimentally is derived mostly from structures similar to these observed in Scenario 1 with either $(3S,3'S)$-AXT or $(3R,3'R)$-AXT H-assemblies interacting with the hydrophobic area in the domain IIIB of BSA with the biggest participation of structures that show considerable helicity. Given that the $(3S,3'S)$-AXT : BSA system always (in all tested cases) behaves consistently and that, for $(3R,3'R)$-AXT : BSA, the initial position of the AXT molecules is essential and the formation of the $(3R,3'R)$-AXT dimer is a rare event, one can rationalize the increased probability of observation of the chiroptical signal characteristic for $(3S,3'S)$-AXT aggregates.

In the case of the *meso* AXT monomer, molecular docking shows a small preference in binding when the S-end is in the binding pocket of albumin (Fig. 6 and Table S2, ESI†). The S-end interacts with two polar amino acids (Arg217 and Lys294), forming a pair of strong H-bonds in the deep region of the binding pocket. This can explain the preferential binding of the S-end compared to the R-end (*ca.* 70% and 30% statistical residence events, respectively). Yet importantly for our
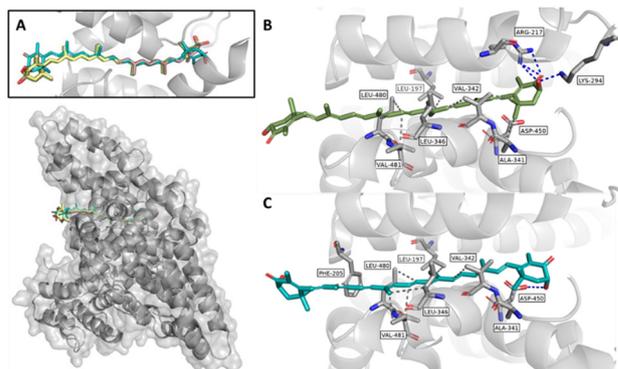

Fig. 6 (**A**) The binding poses (overlapped) of AXT monomers with BSA predicted by molecular docking. Colour codes: $(3S,3'S)$-AXT (yellow), $(3R,3'R)$-AXT (brown) and *meso* AXT (green or turquoise). The best-scored *meso* AXT poses with the S-end (**B**) or the R-end (**C**) in the binding site, with the main interactions stabilizing the protein–ligand complex and crucial amino acid side chains shown as capped sticks.

considerations, there is no significant energy preference of binding of $(3S,3'S)$-AXT or $(3R,3'R)$-AXT to the ligand binding site. Based on Fig. 4C, the ECD signal is derived mostly from $(3S,3'S)$-AXT or $(3R,3'R)$-AXT tightly bound, helical dimers. According to MD simulations (Fig. 5), in all repetitions $(3S,3'S)$-AXT to BSA binding results in the formation of such dimers, but for $(3R,3'R)$-AXT : BSA this probability is 1/3.

This explains why the $(3S,3'S)$-AXT ECD signature is observed more often, when racemic AXT interacts with the protein (Fig. 3C and D). One has also to note, that the experimental systems are even more complicated than our computational models that consider interactions of elements of the racemate with BSA, and not the racemate itself. It is clear from the analysis of the experimental chiroptical spectra of complexes measured for two molar ratios of AXT to BSA equal to 1 : 1 and 3 : 1 that already for the 1 : 1 ratio, the AXT aggregates are formed and their size (hence the chiroptical signal) increases disproportionately for the 3 : 1 ratio of AXT to BSA (as shown by RROA intensity).

This indicates that in real systems, most of the BSA molecules are "empty" and those protein molecules that bind AXT bind a markedly bigger number of carotenoid molecules than is reflected in their stoichiometric ratio. However, it seems that the crucial part is the formation of the initial dimers that (at least for R,R-enantiomer) is an indeterministic process.

With time, these structures aggregate further but their ECD spectrum likely depends on the structure of the initially formed small assembly that dictates helicity. This reasoning can also explain the lack of statistical differences between the 1 : 1 and 3 : 1 systems that show very similar numbers of non-zero intensity *versus* close to zero intensity chiroptical spectra.

4.4. Enantiorecognition in the uptake of AXT by adipocytes

To verify differences in binding of S,S and R,R enantiomers with BSA, not found for enantiopure AXT systems, but evidenced by interactions of the racemate with the protein, we also studied enantioselectivity in the uptake of AXT enantiomers to
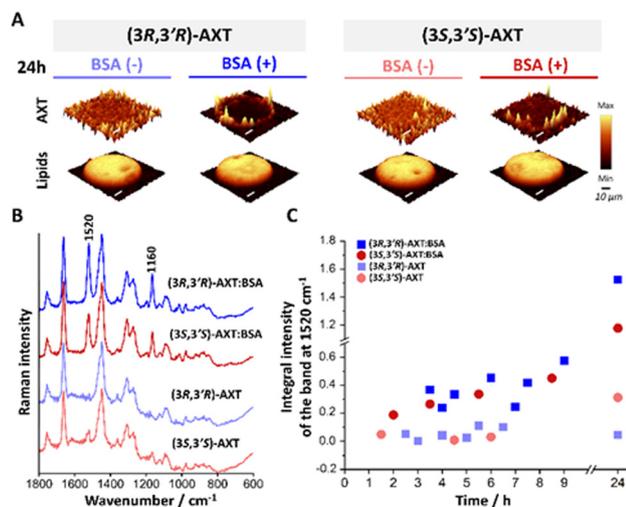
This journal is © the Owner Societies 2025

Phys. Chem. Chem. Phys., 2025, **27**, 4905–4914 | **4911**

Fig. 7 Enantioselectivity in the delivery of AXT *via* albumin to adipocytes. Representative Raman distribution images of AXT and lipids (**A**) and changes in the average cell Raman spectra (**B**) after 24 h incubation of primary adipocytes with AXT complexed with (BSA(+)) or dispersed in THF:water solutions (BSA(−)). Images were obtained by the integration of the marker bands for AXT (1535–1505 cm⁻¹) or lipids (2900–2830 cm⁻¹). The concentration of AXT is 10 μM, and the scale bars are equal to 10 μm. Kinetics of the AXT uptake (**C**) during 24 h incubation.

primary adipocytes. Therefore, $(3S,3'S)$-AXT : BSA and $(3R,3'R)$-AXT : BSA 3 : 1 complexes (spectra in Fig. 1), or monomeric AXT dissolved in THF, were added to the fetal bovine serum (FBS)-free cell cultures. Incubating adipocytes in these media for 24 h

resulted in the Raman distribution images of lipids and AXT presented in Fig. 7A. In the averaged spectra of the cells after incubation with AXT delivered in different forms (Fig. 7B), the bands due to the carotenoid (at 1520 and 1160 cm⁻¹) are clearly less pronounced after incubation with $(3S,3'S)$-AXT : BSA than with $(3R,3'R)$-AXT : BSA or two controls ($(3S,3'S)$-AXT and $(3R,3'R)$-AXT delivered in the solvent). A small (*ca.* 25%) preference has been observed in the delivery of $(3R,3'R)$ enantiomer over $(3S,3'S)$ to adipocytes using albumin (Fig. 7B). Furthermore, the dynamics of the AXT uptake (Fig. 7C) demonstrates that $(3R,3'R)$-AXT is delivered to the cells faster than $(3S,3'S)$-AXT, thus further confirming the enantioselectivity of this process.

A further analysis of the MD simulations provides a plausible explanation for these observations. Fig. 8 and Fig. S8 and S9 (ESI†) show the time evolution of the two main intermolecular interaction energy components—Coulomb and van der Waals (vdW) energies—for the interactions between AXT molecules and between them and BSA. By comparing the AXT–BSA interaction energies between the $(3R,3'R)$ and $(3S,3'S)$ enantiomer systems (Fig. 8, bottom 3 rows), it can be concluded that for the AXT molecules which are outside the binding pocket (AXT2 and AXT3), the AXT···BSA interaction vdW energies are greater in all simulations of the $(3R,3'R)$ system compared to $(3S,3'S)$. This is further corroborated by the count of calculated H-bonds between AXT molecules and between them and BSA, which are shown in Fig. S10–S12 (ESI†). These reveal an enhanced interaction *via* H-bonds between AXT2, AXT3 and BSA for the $(3R,3'R)$ system when compared to $(3S,3'S)$ (Fig. S10
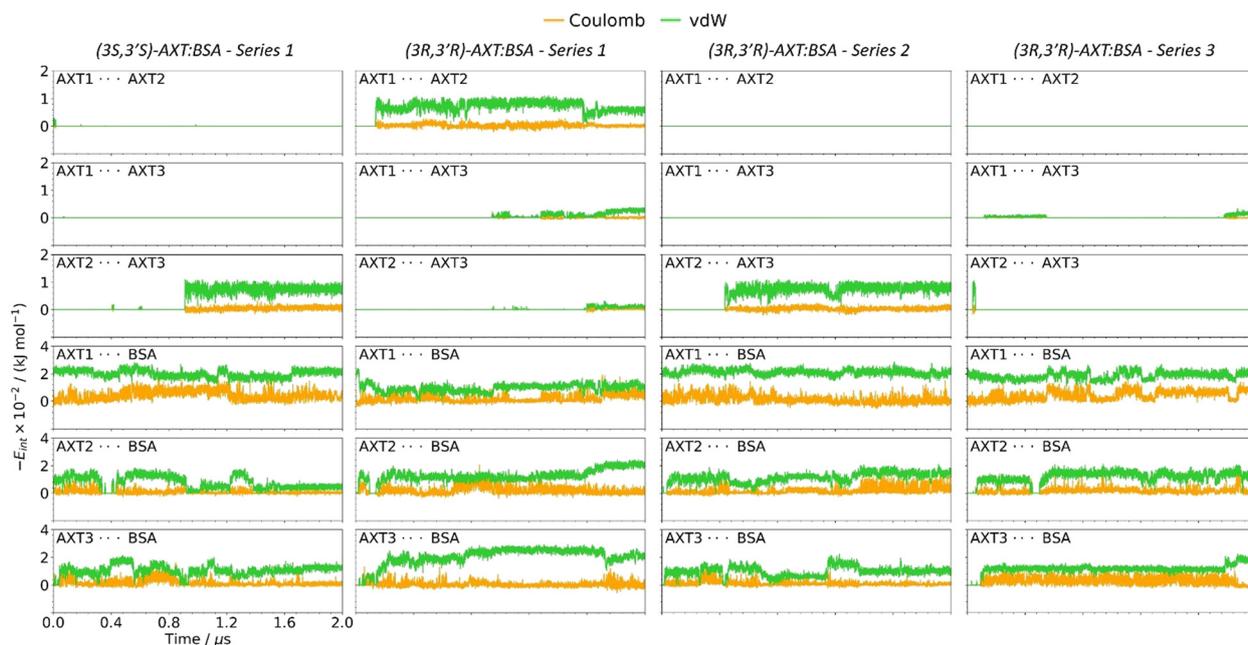

Fig. 8 Coulomb and van der Waals (vdW) interaction energies (see the colour codes on top) within each pair of AXT molecules (three rows on top) as well as between each AXT molecule and the protein (BSA). For both $(3S,3'S)$-AXT : BSA and $(3R,3'R)$-AXT : BSA systems three independent MD series were simulated. In the case of $(3S,3'S)$-AXT : BSA, all three series give similar results and only the results of series 1 are shown (left column). In the case of $(3R,3'R)$-AXT : BSA, all three series give different results and each of the three series is shown. See the legend on top of each column for the identification of each series.

4912 | *Phys. Chem. Chem. Phys.*, 2025, **27**, 4905–4914

This journal is © the Owner Societies 2025

and S11, bottom 2 rows, ESI†). Apart from series 1 simulation of the $(3R,3'R)$ system, no discernible differences could be found in the AXT1···BSA interaction energies between the two enantiopure systems. Indeed, as mentioned before, in the $(3R,3'R)$ series 1 simulation the binding pocket opened, causing AXT1 to migrate outside it, hence the smaller AXT1···BSA interaction energies in this case (Fig. 8, row 4, column 2). However, this also allowed for the formation of a trimer of AXT molecules near the binding pocket, and this weaker interaction is compensated by strong interactions between the AXT molecules and between AXT2, AXT3 and BSA. It is also apparent that the formation of the AXT2–AXT3 dimers is governed by van der Waals and not by Coulomb interactions, as expected, given the mostly apolar nature of these molecules. However, there seems to be no significant difference between the $(3R,3'R)$, $(3S,3'S)$ and $(3R,3'S)$ systems in terms of the magnitude of the interaction energies within these dimers (Fig. 8 and Fig. S8 and S9, ESI†). In fact, Fig. S10–S12 (ESI†) even show that such dimers feature a smaller amount of inter-molecular H-bonds in the case of $(3R,3'R)$ systems, evidencing a smaller proportion of *H*-type aggregates in accordance with Scenario 2 proposed above. Therefore, it is possible that the observed preference for $(3R,3'R)$-AXT delivery could be due to overall more favourable AXT–BSA interactions. It is also worth mentioning that, with the exception of the binding pocket opening occurring in $(3R,3'R)$ series 1, the interactions between AXT and BSA do not cause major changes in the structure of the protein, as evidenced by the relatively stable values of H-bonds (Fig. S13, ESI†) and salt bridges (Fig. S14, ESI†) within BSA, BSA gyration radius (Fig. S15, ESI†) and head-to-tail distance (Fig. S16, ESI†), as well as secondary structure assignments (Fig. S17–S20, ESI†).

5. Conclusions

Our results demonstrate that enantiorecognition can be triggered by the increase of the system complexity.

In the studied racemic AXT-albumin system, we observed a higher intensity of the induced ECD signal of $(3S,3'S)$-AXT as compared with $(3R,3'R)$-AXT. A plausible explanation of this fact was provided by MD simulations. They reveal a unique binding mode of $(3S,3'S)$-AXT form with the protein. On the other hand, the $(3R,3'R)$-AXT form shows multiple (random) possibilities for binding with BSA and has a larger interaction energy with the protein. Hence, this enantiomer is more likely to aggregate with BSA and be transported to fat cells, which has been confirmed by the preferential uptake of $(3R,3'R)$-AXT by adipocytes.

Our observations are particularly important in the context of mutual chiral recognition in protein–drug systems, revealing the inadequacy of simple models in the analysis of the formation of such complex assemblies.

Author contributions

The manuscript was written through contributions from all authors. Conceptualization: A. Kaczor and J. Mazurkiewicz;

separation of AXT isomers: S. Buda; sample preparation and chiroptical studies: J. Mazurkiewicz; cell studies: E. Stanek and J. Mazurkiewicz; molecular docking simulation: M. Karpiel and J. Kalinowska-Tłuścik; molecular dynamics simulation: T. H. Ferreira and P. Maximiano; formal analysis: A. Kaczor (ECD, ROA Raman imaging), J. Mazurkiewicz (ECD, ROA), and E. Stanek (Raman imaging); molecular docking: J. Kalinowska-Tłuścik and M. Karpiel; molecular dynamics: T. H. Ferreira, P. Maximiano and P. N. Simões; data visualization: J. Mazurkiewicz, M. Karpiel, T. H. Ferreira, P. Maximiano, and I. Reva; writing of original draft: J. Mazurkiewicz and A. Kaczor; supervision and project administration: A. Kaczor, P. N. Simões and I. Reva; funding acquisition: J. Mazurkiewicz, A. Kaczor, I. Reva, P. Maximiano and T. H. Ferreira. All authors have given approval to the final version of the manuscript.

Data availability

The data supporting this article have been partially included as part of the ESI.†

Conflicts of interest

There are no conflicts to declare.

Acknowledgements

References

1 A. J. Hutt and S. C. Tan, *Drugs*, 1996, **52**(suppl 5), 1–12.
2 G. K. E. Scriba, *TrAC, Trends Anal. Chem.*, 2019, **120**, 115639.
3 K. M. Koeller and C.-H. Wong, *Nature*, 2001, **409**, 232–240.
4 G. R. Desiraju, *Nature*, 2001, **412**, 397–400.
5 F. García, R. Gómez and L. Sánchez, *Chem. Soc. Rev.*, 2023, **52**, 7524–7548.
6 E. Mattia and S. Otto, *Nat. Nanotechnol.*, 2015, **10**, 111–119.
7 W. Dzwolak, A. Loksztejn, A. Galinska-Rakoczy, R. Adachi, Y. Goto and L. Rupnicki, *J. Am. Chem. Soc.*, 2007, **129**, 7517–7522.
8 N. Hachlica, A. Kolodziejczyk, M. Rawski, M. Górecki, A. Wajda and A. Kaczor, *Spectrochim. Acta, Part A*, 2024, **304**, 123293.
9 A. Loksztejn and W. Dzwolak, *J. Mol. Biol.*, 2008, **379**, 9–16.
10 H.-Y. Chung, A. L. A. Ferreira, S. Epstein, S. A. R. Paiva, C. Castaneda-Sceppa and E. J. Johnson, *Am. J. Clin. Nutr.*, 2009, **90**, 533–539.

11 V. Böhm, G. Lietz, B. Olmedilla-Alonso, D. Phelan, E. Reboul, D. Bánati, P. Borel, J. Corte-Real, A. R. de Lera, C. Desmarchelier, J. Dulinska-Litewka, J. F. Landrier, I. Milisav, J. Nolan, M. Porrini, P. Riso, J. M. Roob, E. Valanou, A. Wawrzyniak, B. M. Winklhofer-Roob, R. Rühl and T. Bohn, *Nutr. Rev.*, 2021, **79**, 544–573.

12 X. Li, G. Wang, D. Chen and Y. Lu, *Food Chem.*, 2015, **179**, 213–221.

13 J. Mazurkiewicz, E. Stanek, A. Kolodziejczyk, M. Karpiel, K. Czamara, T. H. Ferreira, P. Maximiano, P. N. Simões, I. Reva, J. Kalinowska-Tłuścik and A. Kaczor, *Phys. Chem. Chem. Phys.*, 2024, **26**, 7865–7876.

14 E. Reszczynska, R. Welc, W. Grudzinski, K. Trebacz and W. I. Gruszecki, *Arch. Biochem. Biophys.*, 2015, **584**, 125–133.

15 M. J. Abraham, T. Murtola, R. Schulz, S. Páll, J. C. Smith, B. Hess and E. Lindahl, *SoftwareX*, 2015, **1–2**, 19–25.

16 G. Bussi, D. Donadio and M. Parrinello, *J. Chem. Phys.*, 2007, **126**, 014101.

17 S. Nosé and M. L. Klein, *Mol. Phys.*, 1983, **50**, 1055–1076.

18 M. Parrinello and A. Rahman, *J. Appl. Phys.*, 1981, **52**, 7182–7190.

19 J. Huang, S. Rauscher, G. Nawrocki, T. Ran, M. Feig, B. L. de Groot, H. Grubmüller and A. D. MacKerell, Jr., *Nat. Methods*, 2017, **14**, 71–73.

20 K. Vanommeslaeghe, E. P. Raman and A. D. MacKerell, Jr., *J. Chem. Inf. Model.*, 2012, **52**, 3155–3168.

21 S. Jo, T. Kim, V. G. Iyer and W. Im, *J. Comput. Chem.*, 2008, **29**, 1859–1865.

22 N. Hachlica, M. Stefańska, M. Mach, M. Kowalska, P. Wydro, A. Domagała, J. Kessler, G. Zając and A. Kaczor, *Small*, 2024, **20**, 2306707.

23 A. D. MacKerell, D. Bashford, M. Bellott, R. L. Dunbrack, J. D. Evanseck, M. J. Field, S. Fischer, J. Gao, H. Guo, S. Ha, D. Joseph-McCarthy, L. Kuchnir, K. Kuczera, F. T. Lau, C. Mattos, S. Michnick, T. Ngo, D. T. Nguyen, B. Prodhom, W. E. Reiher, B. Roux, M. Schlenkrich, J. C. Smith, R. Stote, J. Straub, M. Watanabe, J. Wiórkiewicz-Kuczera, D. Yin and M. Karplus, *J. Phys. Chem. B*, 1998, **102**, 3586–3616.

24 B. Hess, H. Bekker, H. J. C. Berendsen and J. G. E. M. Fraaije, *J. Comput. Chem.*, 1997, **18**, 1463–1472.

25 T. Darden, D. York and L. Pedersen, *J. Chem. Phys.*, 1993, **98**, 10089–10092.

26 W. Humphrey, A. Dalke and K. Schulten, *J. Mol. Graphics*, 1996, **14**, 33–38.

27 R. Bauernschmitt and R. Ahlrichs, *Chem. Phys. Lett.*, 1996, **256**, 454–464.

28 R. E. Stratmann, G. E. Scuseria and M. J. Frisch, *J. Chem. Phys.*, 1998, **109**, 8218–8224.

29 A. D. Becke, *Phys. Rev. A: At., Mol., Opt. Phys.*, 1988, **38**, 3098–3100.

30 C. Lee, W. Yang and R. G. Parr, *Phys. Rev. B: Condens. Matter Mater. Phys.*, 1988, **37**, 785–789.

31 S. H. Vosko, L. Wilk and M. Nusair, *Can. J. Phys.*, 1980, **58**, 1200–1211.

32 T. Clark, J. Chandrasekhar, G. W. Spitznagel and P. V. R. Schleyer, *J. Comput. Chem.*, 1983, **4**, 294–301.

33 M. J. Frisch, J. A. Pople and J. S. Binkley, *J. Chem. Phys.*, 1984, **80**, 3265–3269.

34 R. Krishnan, J. S. Binkley, R. Seeger and J. A. Pople, *J. Chem. Phys.*, 1980, **72**, 650–654.

35 M. J. Frisch, G. W. Trucks, H. B. Schlegel, G. E. Scuseria, M. A. Robb, J. R. Cheeseman, G. Scalmani, V. Barone, G. A. Petersson, H. Nakatsuji, X. Li, M. Caricato, A. V. Marenich, J. Bloino, B. G. Janesko, R. Gomperts, B. Mennucci, H. P. Hratchian, J. V. Ortiz, A. F. Izmaylov, J. L. Sonnenberg, D. Williams-Young, F. Ding, F. Lipparini, F. Egidi, J. Goings, B. Peng, A. Petrone, T. Henderson, D. Ranasinghe, V. G. Zakrzewski, J. Gao, N. Rega, G. Zheng, W. Liang, M. Hada, M. Ehara, K. Toyota, R. Fukuda, J. Hasegawa, M. Ishida, T. Nakajima, Y. Honda, O. Kitao, H. Nakai, T. Vreven, K. Throssell, J. A. Jr., J. E. Peralta, F. Ogliaro, M. J. Bearpark, J. J. Heyd, E. N. Brothers, K. N. Kudin, V. N. Staroverov, T. A. Keith, R. Kobayashi, J. Normand, K. Raghavachari, A. P. Rendell, J. C. Burant, S. S. Iyengar, J. Tomasi, M. Cossi, J. M. Millam, M. Klene, C. Adamo, R. Cammi, J. W. Ochterski, R. L. Martin, K. Morokuma, O. Farkas, J. B. Foresman and D. J. Fox, *Gaussian 16, Revision C.01*, Gaussian Inc., Wallingford, CT, 2016.

36 R. Dennington, T. A. Keith and J. M. Millam, *GaussView, Version 6.0*, Semichem Inc., Shawnee Mission, KS, 2016.

37 H. M. Berman, J. Westbrook, Z. Feng, G. Gilliland, T. N. Bhat, H. Weissig, I. N. Shindyalov and P. E. Bourne, *Nucleic Acids Res.*, 2000, **28**, 235–242.

38 A. Bujacz, *Acta Crystallogr., Sect. D: Biol. Crystallogr.*, 2012, **68**, 1278–1289.

39 Schrödinger Release 2023-1: Maestro, Schrödinger, LLC, New York, NY, 2023.

40 C. Lu, C. Wu, D. Ghoreishi, W. Chen, L. Wang, W. Damm, G. A. Ross, M. K. Dahlgren, E. Russell, C. D. Von Bargen, R. Abel, R. A. Friesner and E. D. Harder, *J. Chem. Theory Comput.*, 2021, **17**, 4291–4300.

41 M. L. Verdonk, J. C. Cole, M. J. Hartshorn, C. W. Murray and R. D. Taylor, *Proteins*, 2003, **52**, 609–623.

42 M. R. Ashrafi-Kooshk, F. Ebrahimi, S. Ranjbar, S. Ghobadi, N. Moradi and R. Khodarahmi, *Biologicals*, 2015, **43**, 333–343.

43 *The PyMOL Molecular Graphics System, version 2.0*, LLC, 2021.

44 S. Salentin, S. Schreiber, V. J. Haupt, M. F. Adasme and M. Schroeder, *Nucleic Acids Res.*, 2015, **43**, W443–447.

45 M. Dudek, E. Machalska, T. Oleszkiewicz, E. Grzebelus, R. Baranski, P. Szcześniak, J. Mlynarski, G. Zajac, A. Kaczor and M. Baranska, *Angew. Chem., Int. Ed.*, 2019, **58**, 8383–8388.

46 M. Dudek, G. Zajac, A. Kaczor and M. Baranska, *J. Phys. Chem. B*, 2016, **120**, 7807–7814.

47 A. Orlef, E. Stanek, K. Czamara, A. Wajda and A. Kaczor, *Chem. Commun.*, 2022, **58**, 9022–9025.

48 G. Zajac, A. Kaczor, A. Pallares Zazo, J. Mlynarski, M. Dudek and M. Baranska, *J. Phys. Chem. B*, 2016, **120**, 4028–4033.

49 G. Zajac, J. Lasota, M. Dudek, A. Kaczor and M. Baranska, *Spectrochim. Acta, Part A*, 2017, **173**, 356–360.

4914 | *Phys. Chem. Chem. Phys.*, 2025, **27**, 4905–4914

This journal is © the Owner Societies 2025